Nanoscale

Accepted Manuscript

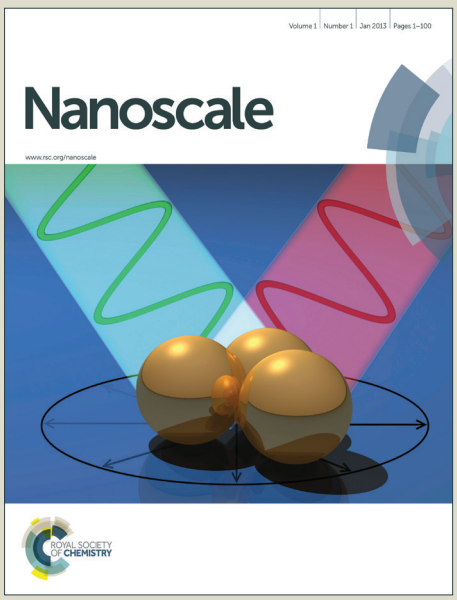

ROYAL SOCIETY OF CHEMISTRY

www.rsc.org/nanoscale

Journal Name

RSCPublishing

ARTICLE

Triangular Ag-Pd alloy Nanoprisms: Rational Synthesis with High-Efficiency for Electrocatalytic Oxygen Reduction

Cite this: DOI: 10.1039/xoxxoooooox

Received ooth January 2012,
Accepted ooth January 2012

DOI: 10.1039/xoxxoooooox

www.rsc.org/

Lin Xu, Zhimin Luo, Zhanxi Fan, Xiao Zhang, Chaoliang Tan, Hai Li, Hua Zhang, and Can Xue*

We report the generation of triangular Ag-Pd alloy nanoprisms through a rationally designed synthetic strategy based on silver nanoprisms as sacrificial templates. The galvanic replacement between Ag nanoprism and H_2PdCl_4 along with co-reduction of Ag^+/Pd^{2+} is responsible for the formation of final prismatic Ag-Pd alloy nanostructures. Significantly, these Ag-Pd alloy nanoprisms exhibited superior electrocatalytic activity for oxygen reduction reaction (ORR) as compared with the commercial Pd/C catalyst. Such a high catalytic activity is attributed to not only the alloyed Ag-Pd composition but also the dominant {111} facets of the triangular Ag-Pd nanoprisms. This work demonstrates the rational design of bimetallic alloy nanostructures with control of selective crystal facets that are critical to achieve high catalytic activity for fuel cell systems.

Introduction

Bimetallic nanostructures have received considerable attentions recently due to their unique optical, magnetic, and catalytic properties, which are not accessible by their monometallic counterparts.[1-3] In particular for noble metals, such as Pd, Pt and Au, alloying a principal scarce noble metal with a secondary abundant metal can not only decrease the usage of the scarce noble metal, but also allow for tuning electronic states of the entire structure,[4-6] which often exhibits superior catalytic properties, including activity, selectivity and durability, when comparing with the monometallic counterpart.[7-9] Considering that the catalytic performance of metal nanostructures is highly dependent on their size, shape, exposed facets and compositions, the exploration of an efficient and simple approach to synthesize bimetallic nanocatalysts with well-defined geometrical architectures is of great significance and thus becomes an intensive research topic. Hitherto, a variety of synthetic strategies, such as galvanic replacement,[10,11] seed-mediated growth,[12,13] and co-reduction,[14,15] have been developed for the preparation of various sophisticated bimetallic nanostructures with controllable shape and composition.

One of the representative applications of noble metal catalyst is electrocatalytic oxygen reduction reaction (ORR), which is of great importance in the cathode reaction of fuel cells. Although platinum-based catalysts exhibit exceptional activity and performance toward ORR,[16] the extremely high cost and limited resources would restrict their practical large-scale commercialization in fuel cells. As one of the alternatives, Pd-based materials have been identified as acceptable electrocatalysts comparable to platinum for ORR in alkaline solutions.[17,18] In addition, Ag, as a less-expensive and relative-abundant metal, exhibits good ORR activity in alkaline media,[19,20] especially for HO_2^- disproportionation.[21,22] Thus the alloy of Ag with Pd would be promising to achieve enhanced catalytic activity with better Pd utilization efficiency,[23,24] and economically desirable since the Pd has much higher (>20 times) cost than Ag.[21]

Herein, we demonstrate the successful synthesis of triangular Ag-Pd alloy nanoprisms by employing Ag nanoprisms as sacrificial templates to define both the morphology and size of the final structures. The synthetic strategy relies on the combination of galvanic replacement between Ag nanoprisms and H_2PdCl_4 and co-reduction of Ag^+ and Pd^{2+} in the reaction system. The prepared Ag-Pd alloy nanoprisms exhibited superior electrocatalytic activity in ORR as compared with the commercial Pd/C catalyst, which might be attributed to the synergistic effects of the Ag-Pd alloyed feature along with the dominantly exposed {111} facets of triangular nanoprisms.

Results and discussion

Structural characterizations of Ag-Pd alloy nanoprisms

For the synthesis of triangular Ag-Pd alloy nanoprisms, uniform triangular Ag nanoprisms with an average edge length of 90 nm (Fig. 1a) were firstly prepared through a photoinduced approach.[25] Then solutions of H_2PdCl_4 and ascorbic acid (AA) were simultaneously introduced into the Ag nanoprism solution through two separate tubes on a programmable syringe pump. During the process, the Ag nanoprisms served as sacrificial templates to form Ag-Pd alloy nanoprisms. The representative transmission electron microscopy (TEM) image of the obtained product (Fig. 1b) indicates that the final structures retain triangular shape with slightly larger edge length as compared with the Ag prism templates. The energy-dispersive spectroscopy (EDS) (Fig. S1) confirms that the as-prepared nanoprisms are composed by Ag and Pd. The measurement by atomic force microscopy (AFM) revealed that the average thickness of the Ag-Pd alloy nanoprisms is ~18 nm (Fig. S2), which is also larger than that of the original Ag prisms (~12 nm, Fig. S3). In addition, the Ag-Pd nanoprisms exhibit darker contrast in the edges relative to the center, implying that the edges are thicker than the interior region, which is also supported by the AFM measurement result (Fig. S2). Moreover, on the surface of Ag-Pd alloy nanoprisms, there are some nanochannels that could increase the specific surface area and allow for the transport of molecules/ions, thus would be of significance to catalytic applications.

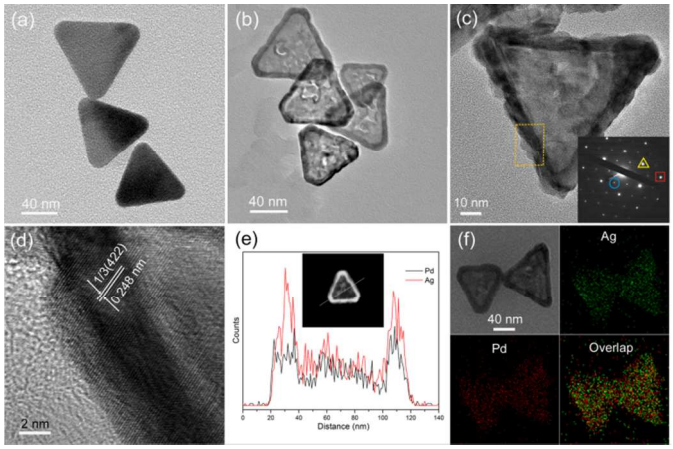

Fig. 1 Characterizations of morphology, structure, and composition of the prepared Ag-Pd alloy nanoprisms. (a) TEM image of the original Ag nanoprisms. (b)-(c) TEM images, (d) HRTEM image, (e) HADDF-STEM image and EDX line profile, and (f) EDX mapping images of Ag-Pd alloy nanoprisms. The inset of (c) shows the SAED pattern of an individual Ag-Pd alloy nanoprism, and the spots (triangular, square and circle) could be indexed to the {220}, {422}, and forbidden 1/3{422} reflections, respectively.

Fig. 1c shows the high-resolution TEM (HRTEM) of a representative Ag-Pd nanoprism. The corresponding selected area electron diffraction (SAED) pattern performed along [111] zone axis indicates three sets of diffraction spots with six-fold rotational symmetry, which can be indexed to the {220}, {422}, and forbidden 1/3{422} reflections, respectively.[26,27] This result is similar to the electron diffraction pattern of the original Ag nanoprism (Fig. S4) and demonstrates the single crystallinity of the Ag-Pd alloy nanoprism. The well-resolved fringes with a lattice spacing of 0.248 nm (Fig. 1d) can be ascribed to the (1/3){422} reflection that is generally forbidden for an *fcc* lattice.

The X-ray diffraction (XRD) pattern (Fig. S5) of the product shows diffraction peaks of typical *fcc*-structured metal. Notably, all peaks are locating between the standard peaks of pure Ag and Pd, and neither an Ag nor Pd single component peak was observed. This result confirms the Ag-Pd alloy phase in the prepared nanoprisms, in line with previous observations in Ag-Pd alloy nanostructures.[15,28,29] The elemental distribution of Ag and Pd in the nanoprism was measured through compositional line profiles and EDX mapping analyses by high-angle annular dark-field scanning TEM (HAADF-STEM). As shown in Fig. 1e, the Ag and Pd traces showed very good matching with two peaks at the edges and one valley in the center. The elemental mapping results (Fig. 1f) indicate that both Ag and Pd are homogeneously distributed throughout the nanoprisms, further confirming the alloy composition. The inductively coupled plasma atomic emission spectroscopy (ICP-AES) reveals that the weight percentage of Pd in the products is 57.7%, suggesting a molar ratio of Ag to Pd as 42: 58.

Morphological evolution and formation mechanism of Ag-Pd alloy nanoprisms

In order to reveal the morphological evolution and understand the formation mechanism of the Ag-Pd alloy nanoprisms, a series of TEM images (Fig. 2) were taken from the intermediate samples collected at different reaction intervals. In the initial reaction stage (t = 45 min, Fig. 2a-2b), the prism template morphology was essentially maintained, and selective Pd deposition on the edges occurred so that the prism edges exhibited darker contrast under TEM observation. When the reaction proceeded further (t = 90 min, Fig. 2c-2d), some areas on the triangular surface displayed less contrast and small pinholes appeared in the prism structure, which is ascribed to the galvanic replacement between H_2PdCl_4 and Ag prisms. After 120-min reaction, Fig. 2e and 2f show that more Ag segments were excavated from the central part, leading to the formation of highly porous structures with pinholes randomly distributed throughout the surface. However, the sample collected at 180-min reaction showed relatively smaller hole regions on the nanoprisms (Fig. 2g-2h), indicating that those pinholes were backfilled. Eventually, upon such continuous backfilling and deposition, as shown in Fig. 2i and 2j, well-developed Ag-Pd alloy nanoprisms were generated after 240-min reaction.

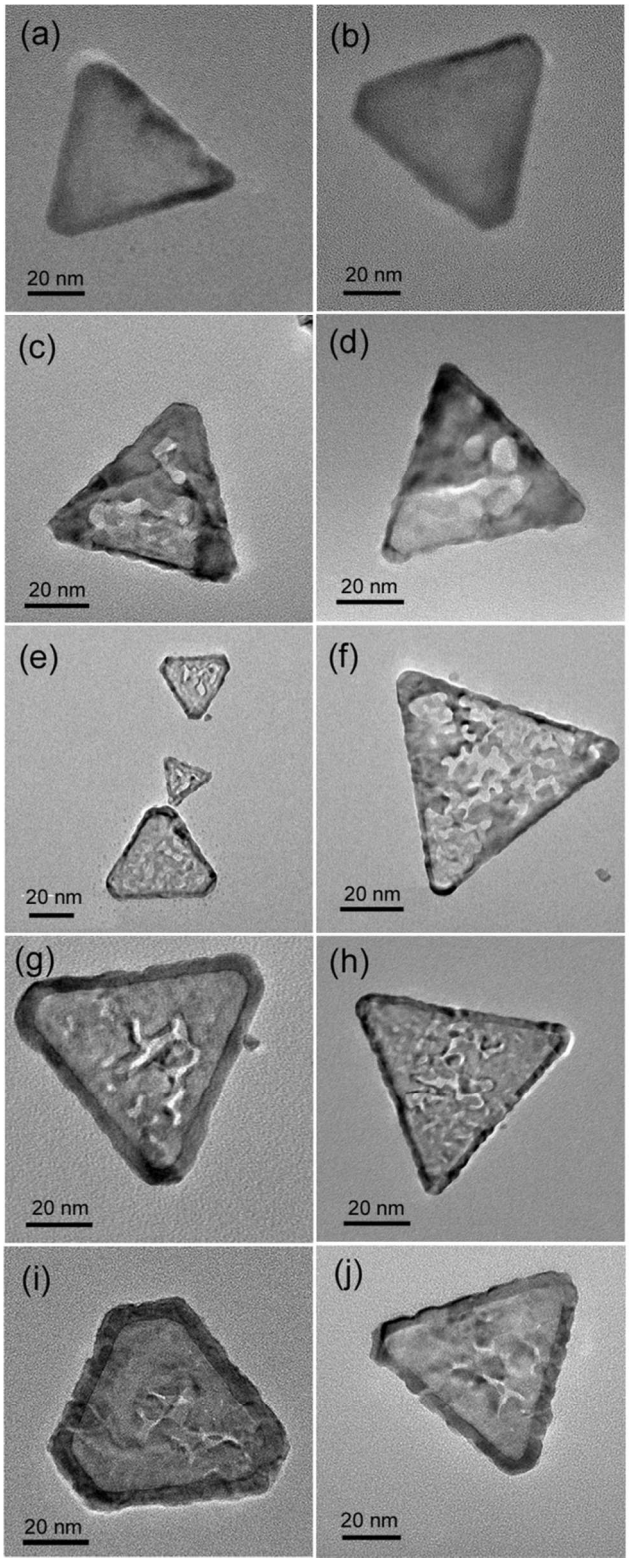

Fig. 2 TEM images of Ag-Pd alloy nanostructures collected at different reaction time: (a)-(b) 45 min, (c)-(d) 90 min, (e)-(f) 120 min, (g)-(h) 180min, and (i)-(j) 240 min.

On the basis of the above observations, we propose the formation mechanism of Ag-Pd alloy nanoprisms as illustrated by Fig. 3. In the present study, Ag nanoprisms are employed as reactive templates for the generation of Ag-Pd alloy nanoprisms. Structural characterizations indicate that each individual Ag nanoprism contains two main {111} facets on the triangular planes and three {110} facets on the edges (Fig. S4). Since the relative surface energies of different crystal facets are in the order of $\gamma_{\{111\}} < \gamma_{\{100\}} < \gamma_{\{110\}}$,[30] and the Pd precursor (H_2PdCl_4) is introduced at a very slow rate through a programmable syringe pump to avoid self-nucleation of Pd^0. Therefore, at the initial reaction stage, the newly formed Pd atoms preferentially nucleate and grow on the prism edges to form Ag@Pd-framed nanoprisms due to the high-energy of {110} facets of Ag nanoprisms. Such initial site-selective Pd deposition on the prism edges is similar to the epitaxial Au growth on the edges of Ag nanoprism.[31-33] Since Ag-Pd system is a well-known binary alloy,[28] the newly formed Pd atoms readily diffuse into the Ag matrix to form seamless and homogeneous Ag-Pd alloys.[34] Because the reduction potential of Pd^{2+}/Pd (0.951 V vs. SHE, SHE = standard hydrogen electrode) is more positive than that of Ag^+/Ag (0.8 V vs. SHE),[35] Ag nanoprisms can be oxidized by H_2PdCl_4. Therefore, owing to the selectively galvanic corrosion on {111} facets,[36,37] some pinholes start to appear preferentially on the triangular face of the nanoprisms as the H_2PdCl_4 concentration increases. These pinholes can further serve as channels of ion transport for the galvanic replacement.

It should be pointed out that the Ag atoms in the newly formed Ag-Pd alloy edges could not be easily oxidized back to Ag^+ through galvanic replacement due to their higher stability than pure Ag atoms in the original nanoprisms.[38] As the reaction proceeded, the Ag {111} facets were gradually removed along with the deposition of more Pd atoms at the edges, creating pinholes on the prism surfaces. At the same time, co-reduction of Pd^{2+} and Ag^+ (from the galvanic replacement) in the solution by AA would occur, leading to backfilling of Ag and Pd atoms as alloys predominantly at the inner edges of the pinholes because these sites possess larger roughness and thus higher surface energy than the outer prism edges and flat surface sites.[31] After the pinholes are backfilled, further deposition of Ag and Pd atoms takes place on all nanoprism surfaces, including tips, edges, and triangular faces. As a result, it finally generated well-developed Ag-Pd alloy nanoprisms. The major structural evolution during the whole reaction is schematically illustrated in Fig. 3.

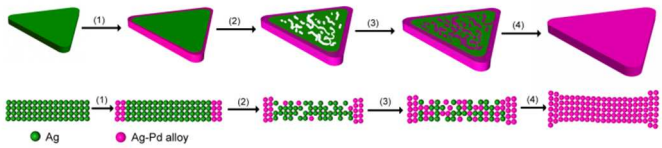

Fig. 3 Schematic illustration of morphological changes in the formation of Ag-Pd alloy nanoprisms from Ag nanoprisms. It involves four major steps: (1) initial deposition of Pd on the Ag nanoprism edges; (2) pinhole generation by dissolution of Ag from {111} facets and simultaneous deposition of Pd on {110} facets; (3) backfilling of the etched pinholes with Ag-Pd alloy; and (4) further deposition on all prism facets that increases both edge length and thickness of the Ag-Pd alloy nanoprisms.

Electrocatalysis activity of Ag-Pd alloy nanoprisms toward ORR

To evaluate the catalytic performance of the prepared Ag-Pd alloy nanoprisms, we investigated the electrocatalytic activity of these structures for oxygen reduction reaction (ORR) in alkaline medium with a rotating disk electrode (RDE). The results are compared with those of commercial Pd/C catalyst (Alfa Aesar, 10 wt%).

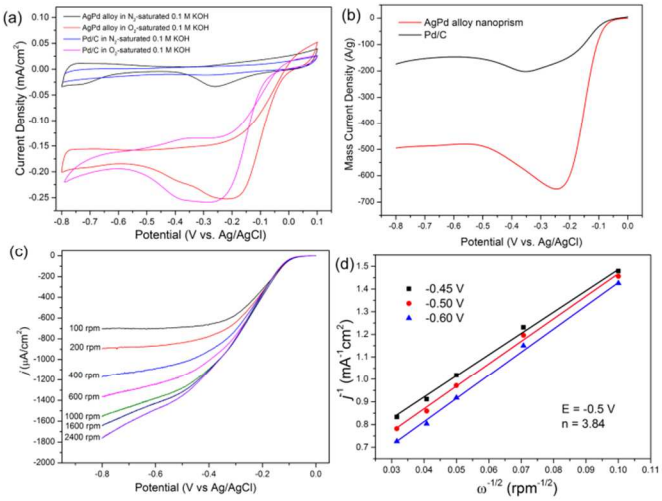

Fig. 4 (a) Typical CVs of the as-prepared Ag-Pd alloy nanoprisms and commercial Pd/C catalyst in N_2-saturated and O_2-saturated 0.1 M KOH solution, respectively. (b) LSV curves of commercial Pd/C catalyst and Ag-Pd alloy nanoprisms. (c) Rotation-disk voltammograms recorded for Ag-Pd alloy nanoprisms supported on a GC electrode in an O_2-saturated 0.1 M KOH solution at a scan rate of 10 mV·s^{-1} at different rotation rates. (d) Koutecky-Levich plot of j^{-1} versus $\omega^{-1/2}$ at different electrode potentials.

Fig. 4a shows the typical cyclic voltammograms (CVs) of the as-prepared Ag-Pd alloy nanoprisms and commercial Pd/C catalyst in N_2-saturated and O_2-saturated 0.1 M KOH solution, respectively. As shown in Fig. 4a, distinct peaks corresponding to oxygen reduction can be observed for both Ag-Pd alloy nanoprisms and the commercial Pd/C catalyst. For commercial Pd/C catalyst, the ORR peak potential located at -0.28 V, while the reduction peak for the Ag-Pd alloy nanoprisms shifts positively to -0.21 V. This result indicates that the prepared Ag-Pd alloy nanoprisms exhibit an enhanced catalytic activity toward ORR in comparison with commercial Pd/C catalyst. Fig. 4b shows the typical linear sweep voltammograms (LSV) curves of commercial Pd/C catalyst and Ag-Pd alloy nanoprisms. The mass-normalized current density generated from Ag-Pd alloy nanoprisms is about 3.2 times higher than that of commercial Pd/C catalyst, which further suggests better ORR catalytic activity of Ag-Pd alloy nanoprisms as compared to the commercial Pd/C catalyst.

The enhanced electrocatalytic performance could be rationally attributed to the alloyed feature of the Ag-Pd nanostructures. It is generally accepted that the common ORR process, as the series 4-electron pathway, should involve both the breaking of an O-O bond and the formation of O-H bonds.[39-41] In the Ag-Pd alloy structure, which has different electronic structure and local reactivity from the monometallic Pd element,[29] the Pd atoms may facilitate the initial oxygen binding, while the Ag may help to desorb the reaction products such as OH^-,[21] resulting in the higher activity in the overall catalytic processes.

Furthermore, the dominance of {111} facets in Ag-Pd alloy nanoprisms also contributes to the enhanced ORR activity. Since all ORR involves both the dissociation of O-O bond and the removal of surface OH groups, the strong adsorption of intermediate OH_{ads} on the catalyst surface would have a negative impact on the catalyst's performance. Owing to the weak interaction between OH_{ads} and {111} facets,[40] the major surfaces of Ag-Pd alloy nanoprisms as {111} facets would have low coverage of OH_{ads}, which promotes the activity for ORR. In addition, due to the porosity feature of the alloy prisms, as shown in Fig. 1b, this structure possesses a relatively high accessible surface area and more catalytically active sites, which are beneficial to enhance the ORR activity. Therefore, on the basis of the aforementioned explanations, the enhanced ORR activity can be reasonably attributed to the synergistic effects of the alloyed composition and dominant {111} facets of triangular Ag-Pd nanoprisms along with the porous features.

The kinetics of ORR catalyzed by Ag-Pd alloy nanoprisms was further studied through measurements with RDE at various rotating speeds. Fig. 4c displays the rotation rate-dependent current density–potential curves. High rotational speeds result in increased oxygen diffusion to electrode surface and large currents. Fig. 4d represents the inverse current density (j^{-1}) at different electrode potentials as a function of the inverse of the square root of the rotation rate ($\omega^{-1/2}$), the so-called Koutecky-Levich (K-L) plot. As shown in Figure 4d, the corresponding K-L curves (j^{-1} versus $\omega^{-1/2}$) at various electrode potentials exhibit good linearity, and the slopes remain almost no change over the potential range from -0.45 to -0.60 V, suggesting that the electron transfer numbers for oxygen reduction at different potentials are similar. The linearity and parallelism of the plots are considered as an indication of first-order reaction kinetics with respect to the concentration of dissolved O_2.[42] From the K-L Equation:[43] $1/j = 1/j_k + 1/(B\omega)^{1/2}$, in which $B = 0.62nFC_0D_0^{2/3}/\nu^{1/6}$ where j is the measured current density, j_k is the kinetic current density, ω is the rotation rate, n is the overall number of electrons transferred in oxygen reduction, F is the Faraday constant (F = 96485 C·mol^{-1}), C_0 is the bulk concentration of O_2 (1.26×10^{-3} mol·L^{-1}), D_0 is the diffusion coefficient of O_2 in the electrolyte (1.93×10^{-5} cm^2·s^{-1}), ν is the viscosity of the electrolyte (0.01 cm^2·s^{-1} in 0.1 M KOH). The number of electrons, n, involved in the ORR was calculated to be 3.84 at -0.5 V, which indicates a nearly four-electron-transfer reaction occurring in the ORR reaction. As such, the as-obtained triangular Ag-Pd alloy nanoprisms with high ORR activity are expected for great applications in fuel cell systems.

Conclusions

In summary, we have demonstrated successful synthesis of triangular Ag-Pd alloy nanoprisms by using Ag nanoprisms as sacrificial templates. The Ag nanoprisms were initially coated with a layer of Pd, followed by the dissolution of Ag from {111} facets due to the galvanic replacement, and then the Ag and Pd atoms backfilled to the {111} facets in a form of alloy via co-reduction of the Ag^{+} and Pd^{2+} by AA. Electrocatalytic tests for ORR indicated that the synthesized Ag-Pd alloy nanoprisms displayed superior activity comparing with the commercial Pd/C catalyst. The enhanced ORR activity is attributed to the synergistic effects of the alloyed composition and dominant {111} facets of the triangular Ag-Pd nanoprisms along with the porous features. This work would be highly impactful to the rational design of future bimetallic alloy nanostructures with high catalytic activity for fuel cell systems.

Experimental

Synthesis of triangular Ag-Pd alloy nanoprisms: Silver nanoprisms were prepared through a photochemical method according to literature protocols (see Supporting Information for details).[31] The as-prepared Ag nanoprism solution (20 mL) was added into 20 mL Millipore water in a glass vial, followed by infusion of 4 mL of 0.3 mM H_2PdCl_4 solution and 4 mL of 8 mM ascorbic acid solution through two separate tubes on a programmable syringe pump. The infusion rate was set as 1.0 $mL{\cdot}h^{-1}$, and the solution was kept vigorous stirring during infusion. The H_2PdCl_4 aqueous solution was prepared by completely dissolving $PdCl_2$ in HCl (0.2 M) at 60 ^{o}C.
Electrochemical measurement: The electrochemical measurements were carried out in a standard three-electrode cell on an Autolab potentiostat/galvanostat electrochemical workstation. The Ag-Pd alloy nanoprisms modified glassy carbon (GC) electrode with a geometric area of 0.071 cm^2 served as a working electrode. For immobilization of nanoparticles, 5 μl solution of Ag-Pd alloy nanopprisms (C_{Pd} = 24.6 μg/ml) was dropped onto the GC electrode and dried under ambient condition. Then 5 μl of Nafion solution (1%) was dropped on the Ag-Pd alloy modified GC electrode to prevent erosion of nanocatalysts during electrochemical measurements. The modified substrate was washed with DI water and dried. Pt wire and Ag/AgCl electrode were used as the counter and reference electrodes, respectively. The electrochemical measurements for oxygen reduction reaction (ORR) were performed in 0.1 M KOH solution. The current density is normalized by the electrode area.

Acknowledgements

This work was financially supported by NTU seed funding for Solar Fuels Laboratory, MOE AcRF-Tier1 (RG 44/11), MOE AcRF-Tier2 (MOE2012-T2-2-041, ARC 5/13), and CRP (NRF-CRP5-2009-04) from NRF Singapore. H.Z. thanks the support from MOE under AcRF Tier 2 (ARC 26/13, MOE2013-T2-1-034) and AcRF Tier 1 (RG 61/12) in Singapore. This research is also funded by the Singapore National Research Foundation and the publication is supported under the Campus for Research Excellence And Technological Enterprise (CREATE) programme (Nanomaterials for Energy and Water Management).

References

School of Materials Science and Engineering
Nanyang Technological University
50 Nanyang Avenue, 639798, Singapore
E-mail: cxue@ntu.edu.sg
Electronic Supplementary Information (ESI) available. See DOI: 10.1039/b000000x/.

1 C. Burda, X. B. Chen, R. Narayanan and M. A. El-Sayed, *Chem. Rev.*, 2005, **105**, 1025.
2 Y. Ding, F. Fan, Z. Tian and Z. L. Wang, *J. Am. Chem. Soc.*, 2010, **132**, 12480.
3 X. Liu, D. Wang and Y. Li, *Nano Today*, 2012, **7**, 448.
4 J. Gu, Y.-W. Zhang and F. Tao, *Chem. Soc. Rev.*, 2012, **41**, 8050.
5 S. U. Son, Y. Jang, J. Park, H. B. Na, H. M. Park, H. J. Yun, J. Lee and T. Hyeon, *J. Am. Chem. Soc.*, 2004, **126**, 5026.
6 N. S. Porter, H. Wu, Z. Quan and J. Fang, *Acc. Chem. Res.*, 2013, **46**,1867.
7 X. Huang, Y. Li, Y. Li, H. Zhou, X. Duan and Y. Huang, *Nano Lett.*, 2012, **12**, 4265.
8 V. Mazumder, M. Chi, M. N. Mankin, Y. Liu, Ö. Metin, D. Sun, K. L. More and S. Sun, *Nano Lett.*, 2012, **12**, 1102.
9 B. Lim, M. Jiang, P. H. C. Camargo, E. C. Cho, J. Tao, X. Lu, Y. Zhu and Y. Xia, *Science*, 2009, **324**, 1302.
10 H. Zhang, M. Jin, J. Wang, W. Li, P. H. C. Camargo, M. J. Kim, D. Yang, Z. Xie and Y. Xia, *J. Am. Chem. Soc.*, 2011, **133**, 6078.
11 W. Zhang, J. Yang and X. Lu, *ACS Nano*, 2012, **6**, 7397.
12 C. J. DeSantis, A. C. Sue, M. M. Bower and S. E. Skrabalak, *ACS Nano*, 2012, **6**, 2617.
13 C. J. DeSantis, A. A. Peverly, D. G. Peters and S. E. Skrabalak, *Nano Lett.*, 2011, **11**, 2164.
14 Y. W. Lee, M. Kim, S. W. Kang and S. W. Han, *Angew. Chem. Int. Ed.*, 2011, **50**, 3466.
15 S. Zhang, Ö. Metin, D. Su and S. Sun, *Angew. Chem. Int. Ed.*, 2013, **52**, 3681.
16 I. E. L. Stephens, A. S. Bondarenko, U. Grønbjerg, J. Rossmeislc and I. Chorkendorff, *Energy Environ. Sci.*, 2012, **5**, 6744.
17 L. Jiang, A. Hsu, D. Chu and R. Chen, *J. Electrochem. Soc.*, 2009, **156**, B643.
18 Y. Bai, R. Long, C. Wang, M. Gong, Y. Li, H. Huang, H. Xu, Z. Li, M. Deng and Y. Xiong, *J. Mater. Chem. A*, 2013, **1**, 4228.
19 B. B. Blizanac, P. N. Ross and N. M. Marković, *J. Phys. Chem. B*, 2006, **110**, 4735.
20 P. Singh and D. A. Buttry, *J. Phys. Chem. C*, 2012, **116**, 10656.
21 D. A. Slanac, W. G. Hardin, K. P. Johnston and K. J. Stevenson, *J. Am. Chem. Soc.*, 2012, **134**, 9812.
22 J. Guo, A. Hsu, D. Chu and R. Chen, *J. Phys. Chem. C*, 2010, **114**, 4324.
23 C.-L. Lee, H.-P. Chiou, C.-M. Syu, C.-R. Liu, C.-C. Yang and C.-C. Syu, *Int. J. Hydrogen Energy*, 2011, **36**, 12706.
24 M. C. Oliveira, R. Rego, L. S. Fernandes and P. B. Tavares, *J. Power Sources*, 2011, **196**, 6092.
25 C. Xue, G. S. Metraux, J. E. Millstone and C. A. Mirkin, *J. Am. Chem. Soc.*, 2008, **130**, 8337.
26 R. Jin, Y. Cao, C. A. Mirkin, K. L. Kelly, G. C. Schatz and J. G. Zheng, *Science*, 2001, **294**, 1901.

27 Y. J. Xiong, I. Washio, J. Y. Chen, H. G. Cai, Z. Y. Li and Y. Xia, *Langmuir*, 2006, **22**, 8563.
28 J. Chen, B. Wiley, J. McLellan, Y. Xiong, Z.-Y. Li and Y. Xia, *Nano Lett.*, 2005, **5**, 2058.
29 Y. Lu and W. Chen, *ACS Catal.*, 2012, **2**, 84.
30 Z. L. Wang, *J. Phys. Chem. B*, 2000, **104**, 1153.
31 M. M. Shahjamali, M. Bosman, S. W. Cao, X. Huang, S. Saadat, E. Martinsson, D. Aili, Y. Y. Tay, B. Liedberg, S. C. J. Loo, H. Zhang, F. Boey and C. Xue, *Adv. Funct. Mater.*, 2012, **22**, 849.
32 M. M. Shahjamali, M. Bosman, S. Cao, X. Huang, X. Cao, H Zhang, S. S. Pramana and C. Xue, *Small*, 2013, **9**, 2880.
33 D. Aherne, D. E. Charles, M. E. Brennan-Fournet, J. M. Kelly and Y. K. Gun'ko, *Langmuir*, 2009, **25**, 10165.
34 E. González, J. Arbiol and V. F. Puntes, *Science* 2011, **334**, 1377.
35 C.-H. Chen, L. S. Sarma, G.-R. Wang, J.-M. Chen, S.-C. Shih, M.-T. Tang, D.-G. Liu, J.-F. Lee, J.-M. Chen and B.-J. Hwang, *J. Phys. Chem. B*, 2006, **110**, 10287.
36 L. Xu, Z. Y. Yin, S. W. Cao, Z. Fan, X. Zhang, H. Zhang and C. Xue, *Chem. Eur. J.,* 2014, **20**, 2742.
37 Q. Zhang, J. Xie, J. Y. Lee, J. Zhang and C. Boothroyd, *Small*, 2008, **4**, 1067.
38 H. Zhang, M. Jin, H. Liu, J. Wang, M. J. Kim, D. Yang, Z. Xie, J. Liu and Y. Xia, *ACS Nano*, 2011, **5**, 8212.
39 V. R. Stamenkovic, B. Fowler, B. S. Mun, G. Wang, P. N. Ross, C. A. Lucas and N. M. Markovic, *Science*, 2007, **315**, 493.
40 J. Yang, J. Yang and J. Y. Ying, *ACS Nano*, 2012, **6**, 9373.
41 N. M. Marković and P. N. Ross, *Surf. Sci. Rep.*, 2002, **45**, 117.
42 R. Liu, D. Wu, X. Feng and K. Müllen, *Angew. Chem.*, 2010, **122**, 2619.
43 A. J. Bard, L. R. Faulkner, *Electrochemical Methods: Fundamentals and Applications*, Wiley, New York, 2001.

